Supplementary Materials
Taylor vortices in yield stress fluids with static wall layers on the outer cylinder

S. TOPAYEV[1], **C. NOUAR**[2] **and I. FRIGAARD**[3]

[1] Zhetysu University named after I. Zhansugurov, 187a Zhansugurova street, 040009 Taldykorgan, Kazakhstan
[2]LEMTA, UMR 7563, CNRS - Université de Lorraine, 2 Avenue de la Fort de Haye, BP 90161, 54505 Vandoeuvre Lès Nancy, France
[3]Department of Mathematics, University of British Columbia, 1984 Mathematics Road, Vancouver, BC, V67 1Z4 Canada

(Received xx; revised xx; accepted xx)

1. Supplementary section: General expression of the yield stress terms $m_{k,ij}$

$$m_{1,ij} = \frac{\dot\gamma_{ij}(\boldsymbol{u})}{\dot\gamma(\boldsymbol{U}_b)} - \frac{\dot\gamma_{ij}(\boldsymbol{U}_b)}{2\dot\gamma^3(\boldsymbol{U}_b)} \sum_{\ell m} \dot\gamma_{\ell m}(\boldsymbol{u})\dot\gamma_{\ell m}(\boldsymbol{U}_b)\,, \tag{1.1}$$

$$m_{2,ij} = \frac{\dot\gamma_{ij}(\boldsymbol{U}_b)}{8} \sum_{k\ell}\sum_{mn} \dot\gamma_{k\ell}(\boldsymbol{u})\dot\gamma_{mn}(\boldsymbol{u}) \left[\frac{3\dot\gamma_{k\ell}(\boldsymbol{U}_b)\dot\gamma_{mn}(\boldsymbol{U}_b)}{\dot\gamma^5(\boldsymbol{U}_b)} - \frac{2}{\dot\gamma^3(\boldsymbol{U}_b)}\frac{\partial\dot\gamma_{k\ell}(\boldsymbol{U}_b)}{\partial\dot\gamma_{mn}(\boldsymbol{U}_b)}\right] - \frac{\dot\gamma_{ij}(\boldsymbol{u})}{2} \sum_{\ell m} \frac{\dot\gamma_{\ell m}(\boldsymbol{u})\dot\gamma_{\ell m}(\boldsymbol{U}_b)}{\dot\gamma^3(\boldsymbol{U}_b)} \tag{1.2}$$

$$\begin{aligned} m_{3,ij} = {} & \frac{\dot\gamma_{ij}(\boldsymbol{u})}{8} \sum_{k\ell}\sum_{mn} \dot\gamma_{k\ell}(\boldsymbol{u})\dot\gamma_{mn}(\boldsymbol{u}) \left[\frac{3\dot\gamma_{k\ell}(\boldsymbol{U}_b)\dot\gamma_{mn}(\boldsymbol{U}_b)}{\dot\gamma^5(\boldsymbol{U}_b)} - \frac{2}{\dot\gamma^5(\boldsymbol{U}_b)}\frac{\partial\dot\gamma_{k\ell}(\boldsymbol{U}_b)}{\partial\dot\gamma_{mn}(\boldsymbol{U}_b)}\right] \\ & + \frac{\dot\gamma_{ij}(\boldsymbol{U}_b)}{48} \sum_{k\ell}\sum_{mn}\sum_{ef} \dot\gamma_{k\ell}(\boldsymbol{u})\dot\gamma_{mn}(\boldsymbol{u})\dot\gamma_{ef}(\boldsymbol{u}) \left[-\frac{15\dot\gamma_{k\ell}(\boldsymbol{U}_b)\dot\gamma_{ef}(\boldsymbol{U}_b)}{\dot\gamma^7(\boldsymbol{U}_b)}\right. \\ & \left. + \frac{6}{\dot\gamma^8(\boldsymbol{U}_b)} \left(\frac{\partial\dot\gamma_{k\ell}}{\partial\dot\gamma_{mn}}(\boldsymbol{U}_b)\dot\gamma_{ef}(\boldsymbol{U}_b) + \frac{\partial\dot\gamma_{ef}}{\partial\dot\gamma_{mn}}(\boldsymbol{U}_b)\dot\gamma_{ef}(\boldsymbol{U}_b) + \frac{\partial\dot\gamma_{mn}}{\partial\dot\gamma_{ef}}(\boldsymbol{U}_b)\dot\gamma_{k\ell}(\boldsymbol{U}_b\right)\right] \end{aligned} \tag{1.3}$$

For clarity, we have made the summations above explicit.

2. Supplementary section: Three-dimensional linear stability analysis

2.1. *Normal mode approach*

The linear system of perturbation equations (3.1)-(3.2) is homogeneous in the axial direction z and the perturbation $(\boldsymbol{u},\, p,\, h)$ is 2π periodic in the azimuthal direction, generic perturbations can therefore be decomposed into Fourier modes with axial wavenumber k and azimuthal wavenumber m:

$$(u,\, v,\, w,\, p,\, h) = (u(r,\, t),\, v(r,\, t),\, w(r,\, t),\, p(r,\, t),\, h(t))\, e^{i(m\theta + k\, z)}. \tag{2.1}$$

The linear system of perturbation equations in Fourier space reads:

$$D_*u + \frac{imv}{r} + ikw = 0\,, \tag{2.2}$$

$$\frac{\partial u}{\partial t} = -Dp - Re_1\,\frac{V_b}{r}\,(imu - 2v) + \left(DD_* - k^2 - \frac{m^2}{r^2}\right)u + B\Phi_r \tag{2.3}$$

$$\frac{\partial v}{\partial t} = -\frac{imp}{r} - Re_1\left(uD_*V_b + imv\frac{V_b}{r}\right) + \left(DD_* - k^2 - \frac{m^2}{r^2}\right)u + \frac{2imu}{r^2} + B\Phi_\theta \tag{2.4}$$

$$\frac{\partial w}{\partial t} = -ikp - Re_1 im\frac{V_b}{r}w + \left(DD_* - k^2 - \frac{m^2}{r^2}\right)w + B\Phi_z\,, \tag{2.5}$$

where

$$\Phi_r = \frac{2}{r}D\left(\frac{rDu}{\dot\gamma_b}\right) + \frac{1}{\dot\gamma_b}\left(ikDw - k^2u - \frac{2\,(imv+u)}{r^2}\right) \tag{2.6}$$

$$\Phi_\theta = \frac{1}{\dot\gamma_b}\left[\frac{2\left(imu - m^2v\right)}{r^2} - \frac{kmw}{r} - k^2v\right]\,, \tag{2.7}$$

$$\Phi_z = \frac{1}{r}D\left(\frac{r\,(iku + Dw)}{\dot\gamma_b}\right) - \frac{1}{\dot\gamma_b}\left(\frac{m^2w}{r^2} + \frac{kmv}{r} + 2k^2w\right)\,. \tag{2.8}$$

In the above equations, $D(.) = d(.)/dr$ and $D_*(.) = d(.)/dr + (.)/r$.
If the fluid is fully yielded in all the annular space, the boundary conditions are:

$$u = v = w = 0 \qquad \text{at} \qquad r = R_1, R_2\,. \tag{2.9}$$

If the fluid is partially yielded, the boundary conditions are

$$u = v = w = 0 \qquad \text{at} \qquad r = R_1, R_y \tag{2.10}$$

We have also to add the compatibility conditions at the yield surface as well as the associated equation to its perturbation h:

$$Du = Dw = 0 \qquad \text{at} \qquad r = R_y\,, \tag{2.11}$$

$$Dv = -hD^2V_b \qquad \text{at} \qquad r = R_y\,. \tag{2.12}$$

In the usual fashion, we consider a normal mode approach and we assume the solution of the form

$$(u, v, w, p, h) = (U_{11}(r), V_{11}(r), W_{11}(r), P_{11}(r), H_{11})\,e^{st}\,. \tag{2.13}$$

The initial value problem (2.3)-(2.5) is transformed into a generalized eigenvalue problem, where the complex frequency s is the eigenvalue. Its real part s_r is the growth rate of the perturbation and its imaginary part s_i is its oscillation frequency. The eigenvalue value problem can be re-written in terms of u and v if $k \neq 0$ or in terms of u and w if $m \neq 0$. The spatial discretization is achieved through a standard Chebyshev spectral collocation method (Schmid & Henningson 2000). At a fixed Re_2, the critical values of the axial wavenumber k and the azimuthal wavenumber m are associated with the minimum value of Re_1 for which $s_{r,max} = 0$ with an accuracy of 10^{-4}. The principle of exchange of stability holds, i.e. $s_i = 0$.

2.2. *Validation of the numerical method used in the linear stability analysis*

The numerical computations were validated by comparison with Agbessi *et al.* (2015), Chen *et al.* (2015), Alibenyahia *et al.* (2012) and Landry *et al.* (2006). As an example of

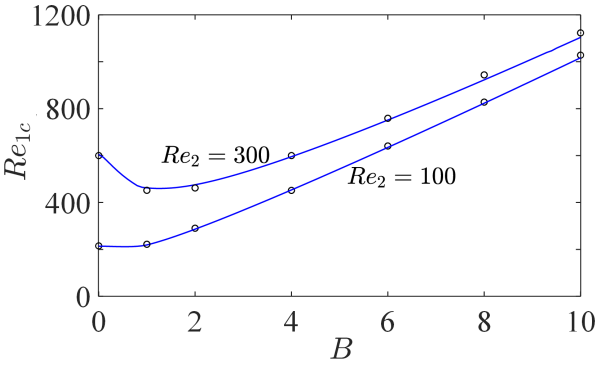

Supplementary Figure 1: Variation of Re_{1c} as a function of B at $\eta = 0.5$ and for $Re_2 = 100, 300$. Our results are in continuous line. The circles are data taken from figure 6a in Landry *et al.* (2006).

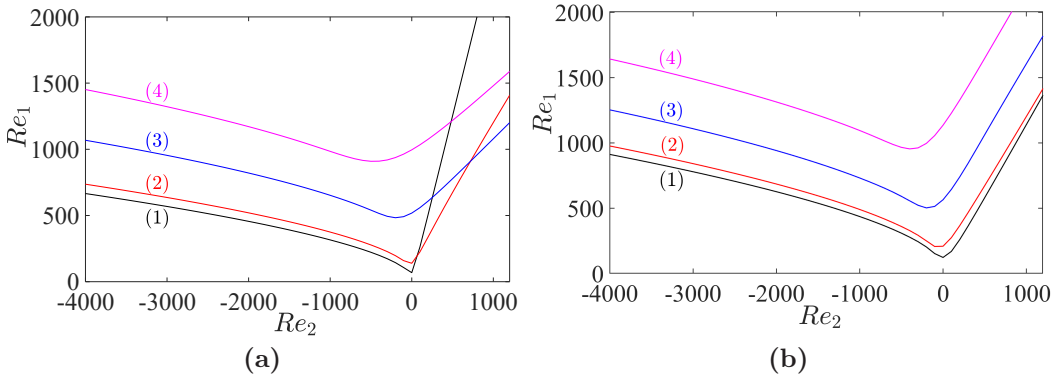

Supplementary Figure 2: Marginal stability curves at (a) $\eta = 0.4$ and (b) $\eta = 0.883$. Effect of Bingham number: (1) $B = 0$, (2) $B = 1$, (3) $B = 5$ and (4) $B = 10$

validation of the numerical procedure used, we have represented in figure 1, the variation of the critical Reynolds number Re_{1c} as a function of the Bingham number at $\eta = 0.5$ and for two values of Re_2: 100 and 300. The convergence of our results has been checked by increasing the number of Chebychev polynoms from $N = 27$ to $N = 41$. The values obtained by Landry *et al.* (2006), read from their figure 6a, are represented by circles. There is a good agreement. The maximum difference is 1% at $Re_2 = 100$ and 2% at $Re_2 = 300$.

2.3. *Results*

Marginal stability curves in the plane (Re_2, Re_1) are shown in figure 2 for a narrow ($\eta = 0.883$) and a wide gap ($\eta = 0.4$). The minimum of the marginal stability curves moves slightly towards counter-rotating cylinders as B increases. It can be observed that for stationary outer cylinder as well as for counter-rotating cylinders, the critical Reynolds number increases monotonically with B for a narrow and a wide gap (see also figure 3(a)). However for co-rotating cylinders, a nonmonotonicity of Re_{1c} is observed as it is illustrated for instance by figure 3(b). For $\eta = 0.4$ and $Re_2 = 300$, Re_{1c} decreases first with increasing B, reaches a minimum at $B = 1.5$ and then increases with B. For a narrow gap, the nonmonotonicity can be observed at much higher outer Reynolds

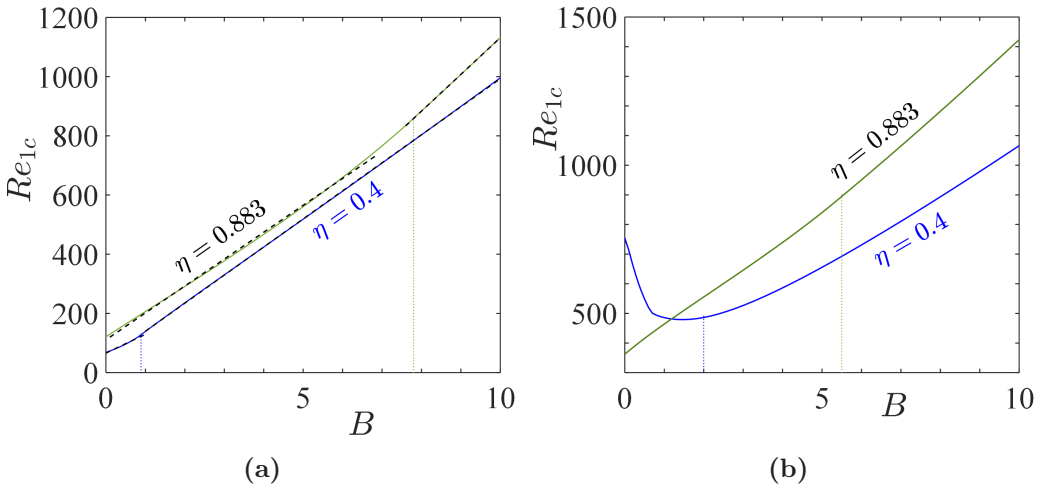

Supplementary Figure 3: Variation of the critical Reynolds number as a function of Bingham number for a wide and a narrow gap: **(a)** case of stationary outer cylinder and **(b)** case of co-rotating cylinders with $Re_2 = 300$.

number ($Re_2 > 2000$).
The co-rotating cylinders is the only one situation where the yield stress has a destabilizing effect for a small-moderate range of B. This result was first observed by Landry (2003) and Peng & Zhu (2004). An explanation based on the energy equation was proposed by Landry *et al.* (2006). Globally, the destabilizing effect corresponds to the situation where the production term in the energy equation is amplified via the increase in the strain-rate at the inner wall and dominates the increase of the viscous dissipation.
Concerning the critical azimuthal and axial wavenumbers (figure 4), for a narrow gap, in the co-rotating regime, the critical mode remains axisymmetric at least up to $Re_2 = 2000$, i.e. the primary bifurcation leads to stationary TVF. In the case of counter-rotating regime, the critical azimuthal wavenumber increases with $|Re_2|$. There is a limit $Re_{2\ell}$ below which the primary bifurcation leads to spiral vortices ($m_c \geqslant 1$). Spiral vortices are traveling waves in axial and azimuthal directions. It is worth noting that when the yield stress is increased, the primary bifurcation remains axisymmetric for a wide range of negative Re_2. The axial wavelength, $\lambda_z = 2\pi/k_c$, decreases with increasingly negative Re_2. This may be attributed to the decrease of the "effective gap" where the Rayleigh instability criterion holds, i.e. the gap between the inner cylinder and the "nodal surface" where $V_b = 0$. Similar trends are observed for a wide gap, except that the axial wavelength is shorter and decreases significantly with increasing Bingham number. This is due to the appearance of a plug zone attached to the outer wall.
Note that for a Newtonian fluid, the linear theory of spiral vortices has been well studied (Krueger *et al.* 1966; Langford *et al.* 1988; Tagg *et al.* 1990; Tagg 1994) and the results are in good agreement with experiments (Snyder 1968; Langford *et al.* 1988). The nonlinear behavior of such vortices has also been investigated by several authors, we cite for instance Demay & Iooss (1984) and Edwards *et al.* (1991).

Some features of the critical mode are shown in figure 5 for Newtonian and Bingham fluids. We have represented contours of the stream function on one wavelength. It can be noted that the isolines are more concentrated near the inner wall with increasing Bingham

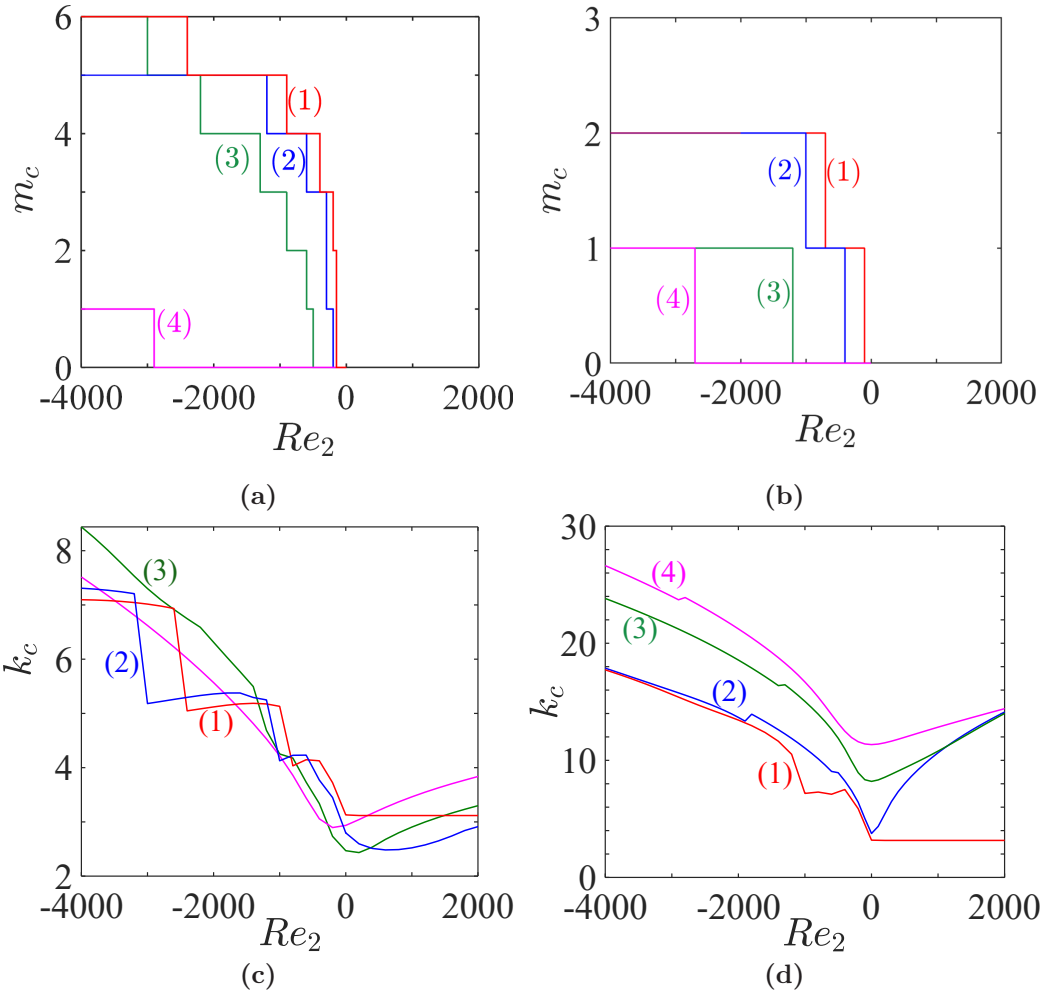

Supplementary Figure 4: Critical azimuthal and axial wave numbers for a Bingham fluid with two radius ratios $\eta = 0.883$ (figures on the left **(a)** and **(c)**) and $\eta = 0.4$ (figures on the right **(b)** and **(d)**). Effect of Bingham number: (1) $B = 0$, (2) $B = 1$, (3) $B = 5$ and (4) $B = 10$.

number, indicating the presence of steep velocity gradient as well as an unaffected plug zone attached to the outer wall.

3. Supplementary section: Operators and matrix coefficients

3.1. *The operator* $\boldsymbol{C}$

$$\boldsymbol{C} = \begin{pmatrix} DD_* + \dfrac{\partial^2}{\partial z^2} & 0 \\ 0 & 1 \end{pmatrix} \tag{3.1}$$

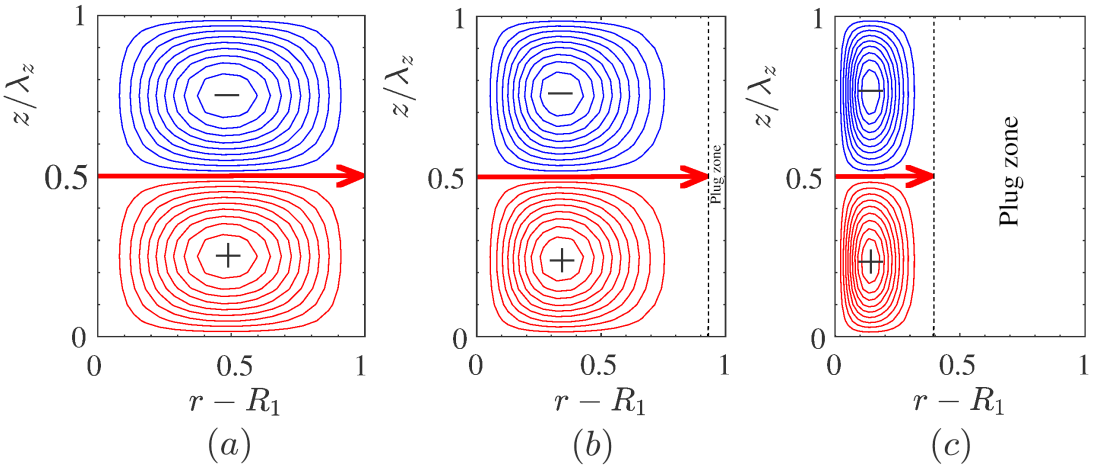

Supplementary Figure 5: Contours of the stream function associated with the critical mode at $Re_2 = 0$, $\eta = 0.4$ for three values of Bingham numbers **(a)** $B = 0$, **(b)** $B = 1$, **(c)** $B = 5$. The arrows indicate the rotation direction of the rolls. (+) clockwise rotation and (-) anti-clockwise rotation

3.1.1. *The sub-scales* $\boldsymbol{C}_0$ *and* $\boldsymbol{C}_1$

$$\boldsymbol{C}_0 \equiv \boldsymbol{C} \quad , \quad \boldsymbol{C}_1 = \begin{pmatrix} 2\dfrac{\partial^2}{\partial z \partial Z} & 0 \\ 0 & 0 \end{pmatrix} \tag{3.2}$$

3.2. *The operator* $\boldsymbol{LI}$

$$\boldsymbol{LI} = \begin{pmatrix} 0 & -2\dfrac{V_b}{r}\dfrac{\partial}{\partial z} \\ D_* V_b \dfrac{\partial}{\partial z} & 0 \end{pmatrix} \tag{3.3}$$

3.2.1. *The sub-scales* $\boldsymbol{LI}_0$, $\boldsymbol{LI}_1$ *and* $\boldsymbol{LI}_2$

$$\boldsymbol{LI}_0 \equiv \boldsymbol{LI} \quad , \quad \boldsymbol{LI}_1 = \begin{pmatrix} 0 & -2\dfrac{V_b}{r}\dfrac{\partial}{\partial Z} \\ D_* V_b \dfrac{\partial}{\partial Z} & 0 \end{pmatrix} \quad , \quad \boldsymbol{LI}_2 = \boldsymbol{0}. \tag{3.4}$$

3.3. *The operator* $\boldsymbol{LV}$

The coefficients of the 2×2 matrix $\boldsymbol{LV}$ are:

$$\boldsymbol{LV} = \begin{pmatrix} \boldsymbol{LV}_{11} & 0 \\ 0 & \boldsymbol{LV}_{22} \end{pmatrix} \tag{3.5}$$

with

$$\boldsymbol{LV}_{11}(\phi) = \left(DD_*\right)^2 \phi + 2\frac{\partial^2}{\partial z^2} DD_*\phi + \frac{\partial^4 \phi}{\partial z^4}, \tag{3.6}$$

$$\boldsymbol{LV}_{22}(v) = \frac{1}{r^2}\frac{\partial}{\partial r}\left[r^2\left(Dv - \frac{v}{r}\right)\right] + \frac{\partial^2 v}{\partial z^2} \tag{3.7}$$

3.3.1. *The sub-scales* $\boldsymbol{LV}_0$, $\boldsymbol{LV}_1$ *and* $\boldsymbol{LV}_2$ *are:*

$$\boldsymbol{LV}_0 \equiv \boldsymbol{LV} \tag{3.8}$$

$$\boldsymbol{LV}_{11}^{(1)}(\phi) = 4DD_*\frac{\partial^2 \phi}{\partial z \partial Z} + 4\frac{\partial^4 \phi}{\partial z^3 \partial Z} \tag{3.9}$$

$$\boldsymbol{LV}_{22}^{(1)}(v) = 2\frac{\partial^2 v}{\partial z \partial Z} \tag{3.10}$$

$$\boldsymbol{LV}_{11}^{(2)}(\phi) = 2DD_*\frac{\partial^2 \phi}{\partial Z^2} + 6\frac{\partial^4 \phi}{\partial z^2 \partial Z^2} \tag{3.11}$$

$$\boldsymbol{LV}_{22}^{(2)}(v) = \frac{\partial^2 v}{\partial Z^2} \tag{3.12}$$

3.4. *The operator* $\boldsymbol{LY}$

$$\boldsymbol{LY} = \begin{pmatrix} \boldsymbol{LY}_{11} & 0 \\ 0 & \boldsymbol{LY}_{22} \end{pmatrix} \tag{3.13}$$

with

$$\boldsymbol{LY}_{11} = \left(DD_* - \frac{\partial^2}{\partial z^2}\right) m_{1,rz} + \frac{\partial}{\partial z}\left(Dm_{1,zz} - D_+ m_{1,rr}\right) + \frac{1}{r}\frac{\partial}{\partial z} m_{1,\theta\theta}\,, \tag{3.14}$$

$$\boldsymbol{LY}_{22} = \frac{\partial}{\partial z} m_{1,\theta z}\,, \tag{3.15}$$

3.4.1. *The sub-scales* $\boldsymbol{LY}_0$, $\boldsymbol{LY}_1$ *and* $\boldsymbol{LY}_2$ *are:*

$$\boldsymbol{LY}_0 \equiv \boldsymbol{LY} \tag{3.16}$$

$$\boldsymbol{LY}_{11}^{(1)}(\phi) = -2DD_*\left(\frac{1}{\dot{\gamma}(\boldsymbol{U}_b)}\frac{\partial^2 \phi}{\partial z \partial Z}\right) - \frac{2}{\dot{\gamma}(\boldsymbol{U}_b)} DD_*\frac{\partial^2 \phi}{\partial z \partial Z} + \frac{4}{\dot{\gamma}(\boldsymbol{U}_b)} \tag{3.17}$$

$$+ 4D\left(\frac{1}{\dot{\gamma}(\boldsymbol{U}_b)} DD_*\frac{\partial^2 \phi}{\partial z \partial Z}\right) + 4D_*\left(\frac{1}{\dot{\gamma}(\boldsymbol{U}_b)}\right) D\frac{\partial^2}{\partial z \partial Z}\frac{\partial^2 \phi}{\partial z \partial Z} \tag{3.18}$$

$$- \frac{4}{r^2 \dot{\gamma}\left(\boldsymbol{U}_b\right)}\,, \tag{3.19}$$

$$\boldsymbol{LY}_{22}^{(1)}(v) = \frac{2}{\dot{\gamma}\left(\boldsymbol{U}_b\right)}\frac{\partial^2 v}{\partial z \partial Z}\,, \tag{3.20}$$

3.5. *The vector* $\boldsymbol{NI}_2$

$$\boldsymbol{NI}_2 = \begin{pmatrix} \boldsymbol{NI}_{2,1} \\ \boldsymbol{NI}_{2,2} \end{pmatrix} \tag{3.21}$$

where,

$$\begin{aligned} \boldsymbol{NI}_{2,1} = & \frac{\partial}{\partial r}\left[\frac{\partial\phi}{\partial z}DD_*\phi - (DD_*\phi)\left(DD_*\frac{\partial\phi}{\partial z}\right)\right] \\ & + \frac{\partial}{\partial z}\left[\frac{\partial\phi}{\partial z}\frac{\partial^2\phi}{\partial r\partial z} - D_*\phi\frac{\partial^2\phi}{\partial z^2} - \frac{v^2}{r}\right], \end{aligned} \tag{3.22}$$

$$\boldsymbol{NI}_{2,2} = \frac{\partial\phi}{\partial z}\frac{\partial v}{\partial r} + \frac{v}{r}\frac{\partial\phi}{\partial z} - D_*\phi\frac{\partial v}{\partial z}. \tag{3.23}$$

4. Supplementary section: Boundary conditions

4.1. *Case* (III) *of base solutions*

In the case where the fluid is fully yielded in the annular space (case III of the base solution), appropriate boundary conditions come from the no-slip conditions at the wall:

$$\boldsymbol{u} = 0 \quad \text{at} \quad r = R_1, R_2\,. \tag{4.1}$$

4.2. *Case* (II) *of base solutions*

In the case where we have a partially yielded fluid, i.e. a case (II) of base solution, the condition (4.1) is satisfied at the inner wall. However, the outer wall is no longer the boundary of the computational domain for the stability problem: it is the yield surface. The yield surface position has been perturbed from R_y to

$$r = R_y + \delta h_1 + \delta^2\bar{h}_2 + \delta^3 h_3 + O(\delta^4)\,. \tag{4.2}$$

Both continuity and yield conditions need to be evaluated at the perturbed yield surface, then linearized onto $r = R_y$.
The continuity of the velocity through the yield surface reads

$$[\boldsymbol{U}_b + \boldsymbol{u}]\left(\left[R_y + \delta h^{(1)} + \delta^2 h^{(2)} + \delta^3 h^{(3)} + ...\right]^-, z, t\right) = [\boldsymbol{U}_b + \boldsymbol{u}]\left(\left[R_y + \delta h^{(1)} + \delta^2 h^{(2)} + \delta^3 h^{(3)} + ..\right.\right.$$

Here the superscripts $\pm$ indicate that the limit is taken from each side of the yield surface. The condition of the velocity continuity has to be linearized onto $r = R_y$. Note that we retain the base flow in these expressions, since the base flow is discontinuous in its second derivative at the yield surface. By continuity from the outer wall, $\boldsymbol{u} = 0$ uniformly within the plug. On writing

$$\boldsymbol{u} = \delta\boldsymbol{u}_1 + \delta^2\boldsymbol{u}_2 + \delta^3\boldsymbol{u}_3 + ... \tag{4.4}$$

the following conditions on the primitive variables are derived at $r = R_y^-$

$$\boldsymbol{u}_1 = \boldsymbol{0}\,, \tag{4.5}$$

$$\boldsymbol{u}_2 = -h_1\frac{\partial\boldsymbol{u}_1}{\partial r} - \frac{h_1^2}{2}\frac{d^2V_b}{dr^2}\boldsymbol{e}_\theta \tag{4.6}$$

$$\boldsymbol{u}_3 = -h_1\frac{\partial\boldsymbol{u}_2}{\partial r} - \bar{h}_2\frac{\partial\boldsymbol{u}_1}{\partial r} - \frac{h_1^2}{2}\frac{\partial^2\boldsymbol{u}_1}{\partial r^2} - h_1\bar{h}_2\frac{d^2V_b}{dr^2}\boldsymbol{e}_\theta - \frac{h_1^3}{6}\frac{d^3V_b}{dr^3}\boldsymbol{e}_\theta\,. \tag{4.7}$$

Additional compatibility conditions are also imposed at the yield surface. Indeed, due to the yield criterion, each component of the strain rate tensor of the perturbed flow vanishes at the yield surface. Expanding both about the base solution and about the base flow yield surface, we obtain the following hierarchical system of compatibility conditions:

$$\dot{\gamma}_{ij}(\boldsymbol{u}_1) = 0 \qquad ij \neq r\theta, \theta r \tag{4.8}$$

$$\dot{\gamma}_{ij}(\boldsymbol{u}_1) + h_1 \frac{\partial}{\partial r}\dot{\gamma}_{ij}(\boldsymbol{U}_b) = 0\,, \qquad ij = r\theta, \theta r\,, \tag{4.9}$$

$$\dot{\gamma}_{ij}(\boldsymbol{u}_2) + h_1 \frac{\partial}{\partial r}\dot{\gamma}_{ij}(\boldsymbol{u}_1) = 0\,, \qquad ij \neq r\theta, \theta r\,, \tag{4.10}$$

$$\dot{\gamma}_{ij}(\boldsymbol{u}_2) + h_1 \frac{\partial}{\partial r}\dot{\gamma}_{ij}(\boldsymbol{u}_1) + h_2 \frac{\partial}{\partial r}\dot{\gamma}_{ij}(\boldsymbol{U}_b) + \frac{h_1^2}{2}\frac{\partial^2}{\partial r^2}\dot{\gamma}_{ij}(\boldsymbol{U}_b) = 0 \qquad ij = r\theta, \theta r \tag{4.11}$$

$$\dot{\gamma}_{ij}(\boldsymbol{u}_3) + h_1 \frac{\partial}{\partial r}\dot{\gamma}_{ij}(\boldsymbol{u}_2) + h_2 \frac{\partial}{\partial r}\dot{\gamma}_{ij}(\boldsymbol{u}_1) + \frac{h_1^2}{2}\frac{\partial^2}{\partial r^2}\dot{\gamma}_{ij}(\boldsymbol{u}_1) = 0 \qquad ij \neq r\theta, \theta r \tag{4.12}$$

$$\dot{\gamma}_{ij}(\boldsymbol{u}_3) + h_1 \frac{\partial}{\partial r}\dot{\gamma}_{ij}(\boldsymbol{u}_2) + h_2 \frac{\partial}{\partial r}\dot{\gamma}_{ij}(\boldsymbol{u}_1) + \frac{h_1^2}{2}\frac{\partial^2}{\partial r^2}\dot{\gamma}_{ij}(\boldsymbol{u}_1) +$$
$$h_3\dot{\gamma}_{ij}(\boldsymbol{U}_b) + h_1 h_2 \frac{\partial^2}{\partial r^2}\dot{\gamma}_{ij}(\boldsymbol{U}_b) + \frac{h_1^3}{6}\frac{\partial^3}{\partial r^3}\dot{\gamma}_{ij}(\boldsymbol{U}_b) = 0 \qquad ij = r\theta, \theta r\,. \tag{4.13}$$

Combining the velocity continuity conditions (4.5-4.7) and yield conditions (4.8-4.13) leads to the following set of conditions at $r = R_y$:

At order δ

$$u_1 = v_1 = w_1 = 0\,, \tag{4.14}$$

$$\frac{\partial u_1}{\partial r} = \frac{\partial w_1}{\partial r} = 0\,, \tag{4.15}$$

$$\frac{\partial v_1}{\partial r} = -h_1 \frac{d^2 V_b}{dr^2}\,. \tag{4.16}$$

At order δ^2

$$u_2 = 0\,, \tag{4.17}$$

$$v_2 = \frac{h_1^2}{2}\frac{d^2 V_b}{dr^2}\,, \tag{4.18}$$

$$w_2 = 0\,, \tag{4.19}$$

$$\frac{\partial u_2}{\partial r} = -h_1 \frac{\partial^2 u_1}{\partial r^2}\,, \tag{4.20}$$

$$\frac{\partial w_2}{\partial r} = -h_1 \frac{\partial^2 w_1}{\partial r^2}\,, \tag{4.21}$$

$$\frac{\partial v_2}{\partial r} = -h_1 \frac{\partial^2 v_1}{\partial r^2} - \bar{h}_2 \frac{d^2 V_b}{dr^2} - \frac{h_1^2}{2}\frac{d^3 V_b}{dr^3} \tag{4.22}$$

At order δ^3

$$u_3 = \frac{h_1^2}{2}\frac{\partial^2 u_1}{\partial r^2}\,, \tag{4.23}$$

$$v_3 = \frac{h_1^2}{2}\frac{\partial^2 v_1}{\partial r^2} + \frac{h_1^3}{3}\frac{d^3 V_b}{dr^3} + h_1\bar{h}_2\frac{d^2 V_b}{dr^2},, \tag{4.24}$$

$$w_3 = \frac{h_1^2}{2}\frac{\partial^2 w_1}{\partial r^2}\,, \tag{4.25}$$

$$\frac{\partial u_3}{\partial r} = -h_1\frac{\partial^2 u_2}{\partial r^2} - \bar{h}_2\frac{\partial^2 u_1}{\partial r^2} - \frac{h_1^2}{2}\frac{\partial^3 u_1}{\partial r^3}\,, \tag{4.26}$$

$$\frac{\partial v_3}{\partial r} = -h_1\frac{\partial^2 v_2}{\partial r^2} - \bar{h}_2\frac{\partial^2 u_1}{\partial r^2} - \frac{h_1^2}{2}\frac{\partial^3 u_1}{\partial r^3} - \frac{h_1\bar{h}_2}{R_0}\frac{d^2 V_b}{dr^2} - h_1\bar{h}_2\frac{d^3 V_b}{dr^3} - \frac{h_1^3}{6R_0}\frac{d^3 V_b}{dr^3}, \tag{4.27}$$

$$\frac{\partial w_3}{\partial r} = -h_1\frac{\partial^2 w_2}{\partial r^2} - \bar{h}_2\frac{\partial^2 w_1}{\partial r^2} - \frac{h_1^2}{2}\frac{\partial^3 w_1}{\partial r^3} \tag{4.28}$$

5. Supplementary section: Validation of procedure used in the weakly nonlinear analysis

In figure 6(a), the radial velocity profile obtained for a Newtonian fluid with $\eta = 0.5$ is compared with that obtained by Fasel & Booz (1984) using a direct numerical simulation. The outer cylinder is fixed and $Re_1 = 72.5$ which corresponds to a relative distance to the onset of vortices $\epsilon = 6.3\%$. The maximum difference is 2.5%. In figure 6(b), the radial velocity variation along the axial line through a vortex center obtained for a Bingham fluid with $B = 0.8547$ is compared with that obtained numerically by Jeng & Zhu (2010). The radius ratio is $\eta = 0.5$ $Re_{1c} = 117.008$ and $\epsilon = 2.56\%$. The maximum difference is 5.5%. Note that for these parameters, the fluid in the annular space is fully yielded. It is also interesting to note in figure 6(b), that the radial outflow ($u > 0$) is narrower and stronger than that corresponding inflow ($u < 0$).
Hence, it appears that for a Newtonian and Bingham fluid, a good agreement is found with the literature.

6. Supplementary section: Comparison between the contributions of non-homogeneous boundary conditions and non-linear inertia terms to the value of the Landau constant.

In figure 7, the contribution of nonhomogeneous boundary condition, g_{1NH} to the value of the Landau constant is compared to that of nonlinear inertial terms g_{1I}. It can be observed that g_{1NH} is almost 10^3 times smaller than $-g_{1I}$.

7. Supplementary section: Contributions of nonlinear inertial and nonlinear yield stress terms

According to equation (4.55), g_{1I} and g_{1Y} can be written formally as

$$g_{1I} = g_{1I}^{1,0} + g_{1I}^{-1,2}, \qquad g_{1Y} = g_{1Y}^{1,0} + g_{1Y}^{-1,2} + g_{1I}^{1,1,-1}, \tag{7.1}$$

where $g_{1I}^{1,0}$ and $g_{1Y}^{1,0}$ are the feedback of the mean flow correction onto the fundamental mode through the nonlinear inertial and nonlinear yield stress terms, respectively, $g_{1I}^{-1,2}$ and $g_{1Y}^{-1,2}$ are the feedback of the second harmonic onto the fundamental mode, etc...A detailed study of these terms is given in table 1. The data show that the feedback of the mean flow correction onto the fundamental mode plays an important role.

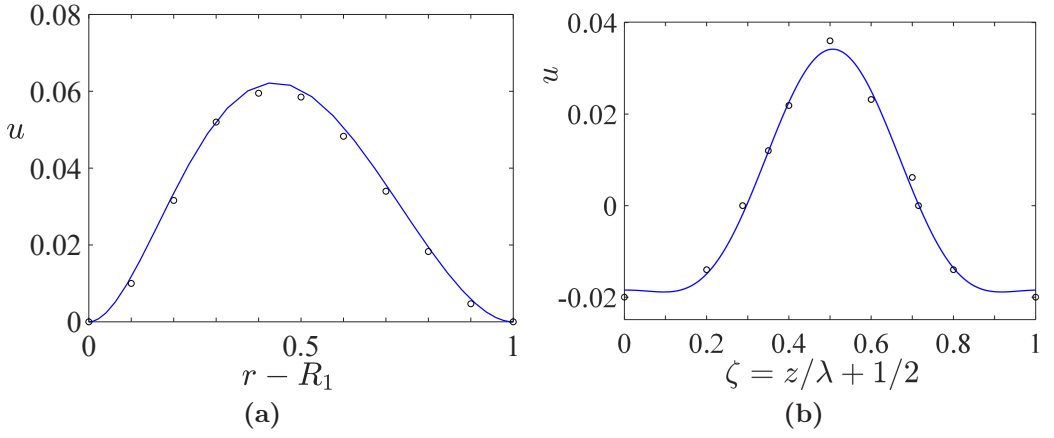

Supplementary Figure 6: **(a)** Radial velocity profile in Newtonian fluid fluid with $\eta = 0.5, Re_2 = 0, Re_1 = 72.5, \epsilon = 6.3\%$ at $z = 0$: (continuous line) our results, (circles) Fasel & Booz (1984) results. **(b)** Radial velocity along the axial line through a vortex center in a Bingham fluid with $\eta = 0.5, B \times Re_{1c} = 100$, $Re_1 = 120$: (continuous line) our results, (circles) Jeng & Zhu (2010) results. Here $\lambda = 2\pi/k_c$.

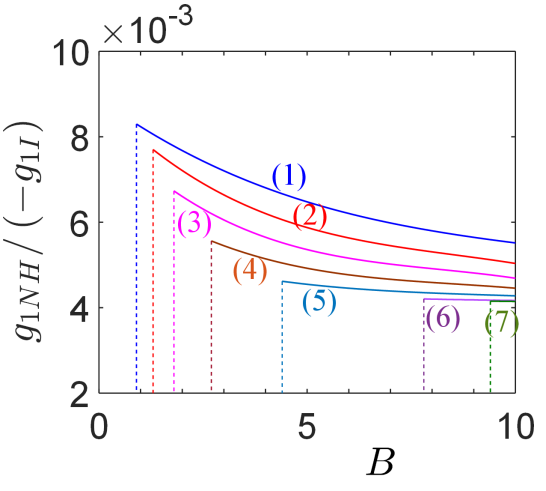

Supplementary Figure 7: The ratio $g_{1NH}/(-g_{1I})$ as a function of B for different radius ratios: (1) $\eta = 0.4$, (2) $\eta = 0.5$, (3) $\eta = 0.6$, (4) $\eta = 0.7$, (5) $\eta = 0.8$, (6) $\eta = 0.883$ and (7) $\eta = 0.9$. The vertical dashed line represents the value of B from which a static layer appears on the outer wall. Before these dashed lines $g_{1NH} = 0$.

8. Supplementary section: Variation of η_ℓ as a function of Re_2

Variation of the radius ratio limit η_ℓ above which the primary bifurcation remains supercritical, as a function of Re_2 in co- and counter-rotation of the outer cylinder.

B	g_1	g_1^I	g_1^V	g_{12}^I	g_{12}^V	g_{10}^I	g_{10}^V	g_{1-11}^V
0.0	-874.785	-874.785	0	-236.14	0	-637.69	0	0
0.5	-1061.4	-1257.2	195.79	-470.14	222.41	-787.07	106.53	-133.14
1.0	-414.4	-1781.5	1367.1	-686.81	621.76	-1094.6	1136.8	-391.46
2.0	-321.2	-2837	2515.8	-944.78	1138.3	-1892.3	2133.1	-755.58
3.0	-186.9	-3865.4	3678.5	-1168.3	1669.3	-2697.1	3150.9	-1141.7
4.0	-34.2	-4893.1	4858.9	-1374	2219.4	-3519.1	4188.9	-1549.5
5.0	127.1	-5929.5	6056.6	-1568.8	2789.2	-4360.7	5244.7	-1977.3
6.0	290.9	-6979.2	7270.1	-1756	3377.7	-5223.2	6315.6	-2423.3
7.0	459.7	-8041.9	8501.6	-1938.9	3986.3	-6103	7402.1	-2886.8
8.0	623.2	-9121.9	9745.1	-2117.6	4611.7	-7004.3	8498.8	-3365.5
9.0	790	-10216	11006	-2294.2	5255.6	-7922.3	9609.4	-3859.4
10.0	952	-11327	12279	-2469	5916.6	-8857.7	10729	-4366.9

Table 1: The first Landau constant g_1 and the contributions of nonlinear inertial and nonlinear viscous terms for different values of the Bingham number. The radius ratio $\eta = 0.5$.

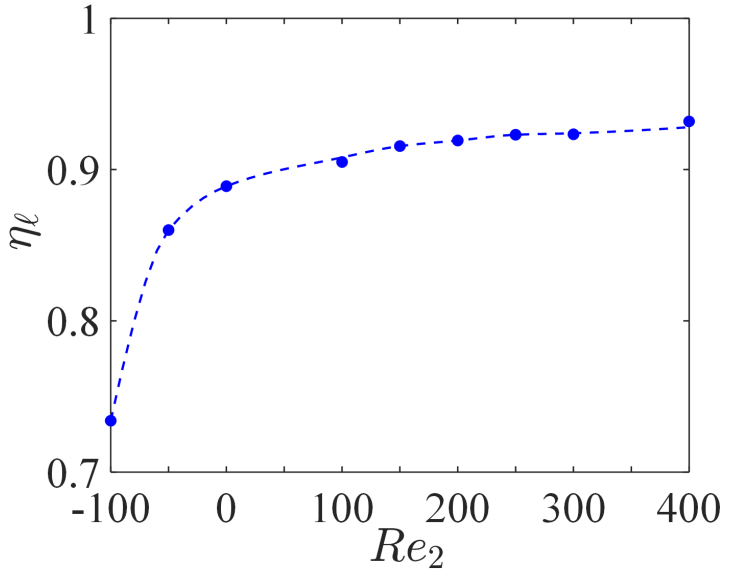

Supplementary Figure 8: Variation of the radius ratio limit η_ℓ above which the primary bifurcation remains supercritical, as a function of Re_2.

9. Supplementary section: Torque

The determination of the torque $\hat{T}$ applied on the inner cylinder is of great interest. It provides information about the energy dissipation. Dubrulle & Hersant (2002) and Eckhardt *et al.* (2007) defined a dimensionless torque as the ratio of $\hat{T}$ to a nominal torque $2\pi\hat{\rho}\hat{\nu}^2\hat{\ell}$, where $\hat{\nu}$ is the kinematic viscosity and $\hat{\ell}$ the height of the inner cylinder immersed in the fluid. By analogy with the heat transfer in Rayleigh-Bénard convection,

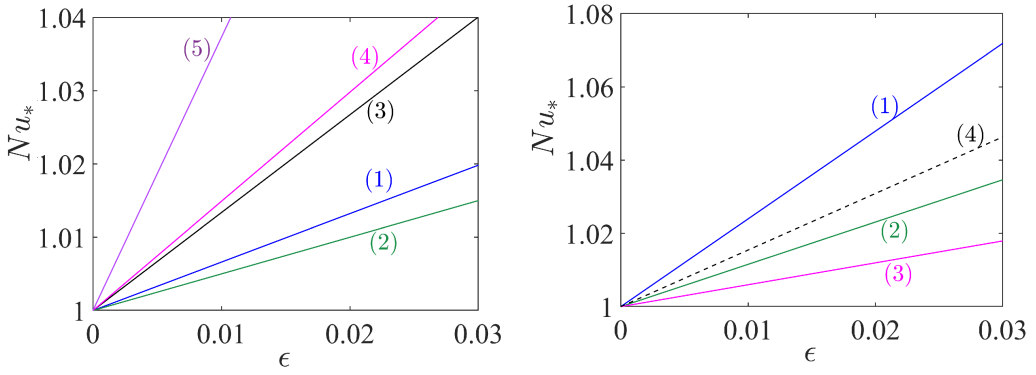

Supplementary Figure 9: Torque applied on the inner cylinder as a function of ϵ at different values of B. **(a)** Wide gap $\eta = 0.4$: (1) $B = 0$, (2) $B = 0.5$, (3) $B = 0.9$, (4) $B = 1$ and (5) $B = 2$. **(b)** Narrow gap $\eta = 0.883$: (1) $B = 0$, (2) $B = 1$, (3) $B = 5$, (4) $B = 7.2$.

the previous authors defined a pseudo-Nusselt number, Nu_* for a Taylor Couette flow as the ratio of G to the dimensionless torque evaluated in the laminar regime G_b:

$$Nu_* = \frac{G}{G_b} = \frac{\int_0^{2\pi/k_c} \left(\tau_{r\theta}\left(\boldsymbol{U}_b + \boldsymbol{u}\right)\right)_{R_1} \mathrm{d}z}{\left(2\pi/k_c\right)\left(\tau_{r\theta}\left(\boldsymbol{U}_b\right)\right)_{R_1}}, \tag{9.1}$$

where

$$\tau_{r\theta}\left(\boldsymbol{U}_b + \boldsymbol{u}\right) = \tau_{r\theta}\left(\boldsymbol{U}_b\right) + \dot{\gamma}_{r\theta}(\boldsymbol{u}) + B\, m1_{r\theta}(\boldsymbol{u}) + B\, m2_{r\theta}\left(\boldsymbol{u}, \boldsymbol{u}\right) + O(|A|^4)\,. \tag{9.2}$$

The pseudo-Nusselt number, Nu_*, represents the dimensionless angular velocity flux or momentum flux (Eckhardt *et al.* 2007). Greater Nu_* implies that that the torque per unit height or the momentum flux is larger.
In the laminar regime, the radial flux of the angular momentum is diffusive and $Nu_* = 1$. In the TVF regime, using equations (2.28), (2.30), (2.31) and (2.33), Nu_* can be written as

$$Nu_* = 1 + \left[\frac{DV_{02}}{\tau_{r\theta}\left(\boldsymbol{U}_b\right)}\right]_{R_1} |A|^2 - Bsgn\left(\dot{\gamma}_{r\theta}\left(\boldsymbol{U}_b\right)\right)\left[\frac{|D^2F_{11}|^2}{\tau_{r\theta}\left(\boldsymbol{U}_b\right)\left[\dot{\gamma}\left(\boldsymbol{U}_b\right)\right]^2}\right]_{R_1} |A|^2 + O\left(|A|^4\right). \tag{9.3}$$

In the case where $k = k_c$, using equation (5.2), the pseudo-Nusselt number can be written formally as:

$$Nu_* = 1 + K\epsilon, \tag{9.4}$$

where K depends on Bingham number. For a Newtonian fluid, we have

$$K = -\frac{1}{\tau_0 g_1}\left[\frac{DV_{02}}{\dot{\gamma}_{r\theta}\left(\boldsymbol{U}_b\right)}\right]_{R_1} \quad \text{with} \quad \left(\dot{\gamma}_{r\theta}\left(\boldsymbol{U}_b\right)\right)_{R_1} = -\frac{2}{\eta\left(1+\eta\right)} \tag{9.5}$$

Figure 9 shows the variation of Nu_* as a function of the distance to the onset of vortices for a wide and a narrow gap at different values of B. Again we find the same trends as in the description of the flow structure. Namely, the nonlinear inertial terms, which are dominant for weak values of B have a stabilising effect, and as soon as the nonlinear

yield stress terms become more important, the torque applied to the inner cylinder increases strongly. Furthermore, the numerical results show that the increase in $Nu*$ is due to the term DV_{02}, which is a correction second order correction in amplitude of the azimuthal profile of the base state. The contribution of the third term in equation (9) is quite weak.

Remark

The term pseudo-Nusselt number was introduced by Eckhardt, Grossmann and Lohse (Europhys. Lett. 2007, J. Fluid Mech. 2007) to describe the analogy between the heat transport in Rayleigh-Bnard convection and the transport of angular momentum in a Taylor-Couette flow. Indeed, in the same way that we define a Nusselt number in a Rayleigh-Bénard convection as the ratio between the heat flux across the fluid layer to that obtained when the fluid is static (diffusive flux), Eckhardt, Grossmann and Lohse (2007a, 2007b) define a pseudo-Nusselt number as the ratio of the angular momentum flux to that obtained in a laminar regime (diffusive flux). This theory describes an angular momentum, which is constant over all radii with

$$J_w = r^3 \left(\langle u\,\omega \rangle_{A,t} - \nu\, \partial_t \langle \omega \rangle_{A,t} \right) \tag{9.6}$$

where the brackets $\langle . \rangle_{A,t}$ describe a mean over a cylindrical surface at radius r over time. In equation (9.6), ν is the kinematic viscosity and ω, the angular velocity. At the inner wall ($r = R_1$), the first part of this equation equals zero ($u = 0$). The second one corresponds to a linear function of the torque $\mathcal{C}$. The ratio of the dimensionless torque (denoted G in the first version) to that obtained in laminar regime (denoted G_b in the first version) is the pseudo-Nusselt number.

REFERENCES

Agbessi, Y., Alibenyahia, B., Nouar, C., Lemaitre, C. & Choplin, L. 2015 Linear stability of Taylor–Couette flow of shear-thinning fluids: modal and non-modal approaches. *J. Fluid Mech.* **776**, 354–389.

Alibenyahia, B., Lematre, C., Nouar, C. & Ait-Messaoudene, N. 2012 Revisiting the stability of circular Couette flow of shear-thinning fluids. *J. Non-Newtonian Fluid Mech.* **183**, 37–51.

Chen, C., Wan, Z-H. & Zhang, W-G. 2015 Transient growth in Taylor-Couette flow of a Bingham fluid. *Phys. Rev. E* **91** (4), 043202.

Demay, Y. & Iooss, G. 1984 Calcul des solutions bifurquées pour le problème de Couette-Taylor avec les deux cylindres en rotation. *J. Mec. Theor. Appl.* pp. 193–216.

Dubrulle, B. & Hersant, F. 2002 Momentum transport and torque scaling in Taylor-Couette flow from an analogy with turbulent convection. *Eur. Phys. J-B* **26** (3), 379–386.

Eckhardt, B., Grossmann, S. & Lohse, D. 2007 Torque scaling in turbulent Taylor–Couette flow between independently rotating cylinders. *J. Fluid Mech.* **581**, 221–250.

Edwards, W.S., Tagg, R., Dornblaser, B.C., Swinney, H.L. & Tuckerman, L.S. 1991 Periodic traveling waves with nonperiodic pressure. *Eur. J. Mech. B/Fluids* **10** (2), 205–210.

Fasel, H & Booz, O 1984 Numerical investigation of supercritical Taylor-vortex flow for a wide gap. *J. Fluid Mech.* **138**, 21–52.

Jeng, J. & Zhu, K.Q. 2010 Numerical simulation of Taylor Couette flow of Bingham fluids. *J. Non-Newtonian Fluid Mech.* **165** (19-20), 1161–1170.

Krueger, E.R., A. Gross, A & DiPrima, R.C. 1966 On the relative importance of Taylor-vortex and non-axisymmetric modes in flow between rotating cylinders. *J. Fluid. Mech.* **24** (3), 521–538.

Landry, M.P. 2003 Taylor-Couette instability of a Bingham fluid. PhD thesis, University of British Columbia.

Landry, M.P., Frigaard, I.A. & Martinez, D.M. 2006 Stability and instability of Taylor–Couette flows of a Bingham fluid. *J. Fluid Mech.* **560**, 321–353.

Langford, W.F., Tagg, R., Kostelich, E.J., Swinney, H.L. & Golubitsky, M. 1988 Primary instabilities and bicriticality in flow between counter-rotating cylinders. *Phys. Fluids* **31** (4), 776–785.

Peng, J. & Zhu, K-Q. 2004 Linear stability of Bingham fluids in spiral Couette flow. *J. Fluid Mech.* **512**, 21–45.

Schmid, P.J. & Henningson, D.S. 2000 *Stability and transition in shear flows*, , vol. 142. Springer Science & Business Media.

Snyder, H.A. 1968 Stability of rotating Couette flow. i. asymmetric waveforms. *Phys. Fluids* **11** (4), 728–734.

Tagg, R. 1994 The Couette-Taylor problem. *Nonlinear Science Today* **4** (3), 1–25.

Tagg, R., Edwards, W.S. & Swinney, H.L. 1990 Convective versus absolute instability in flow between counterrotating cylinders. *Phys. Rev. A* **42** (2), 831.